Research Article | Vol. 28, No. 17 / 17 August 2020 / Optics Express 24389
Optics EXPRESS

Spatial distribution of electric-field enhancement across the gap of terahertz bow-tie antennas

MATTHIAS RUNGE,* DIETER ENGEL, MICHAEL SCHNEIDER, KLAUS REIMANN, MICHAEL WOERNER, AND THOMAS ELSAESSER

Max-Born-Institut für Nichtlineare Optik und Kurzzeitspektroskopie, Max-Born-Strasse 2a, 12489 Berlin, Germany
runge@mbi-berlin.de

Abstract: The electric-field enhancement in terahertz (THz) antennas designed for nonlinear THz spectroscopy of soft matter is characterized by spatially resolved electrooptic sampling. To mimic the relevant interaction geometry, metallic, resonant bow-tie antennas are deposited on a thin zinc telluride crystal of 10 μm thickness. The THz electric field transmitted through the antenna gap is recorded by electrooptic sampling. By focusing the 800 nm, sub-20 fs sampling pulses, we achieve a spatial resolution of some 3 μm, which is 1/3 to 1/8 of the antenna-gap width. The THz field in the gap displays an enhancement by a factor of up to 4.5 with a pronounced spectral variation, depending sensitively on the antenna-arm length and the gap width. By scanning the 800 nm probe spot laterally through the antenna gap, the spatial variation of the enhancement is determined, reaching the highest values at the edges of the gap. The results are in agreement with simulations of the electric-field distributions by finite-element calculations.

1. Introduction

Antennas transform electromagnetic waves into oscillating electric currents and vice versa. While traditional antenna research and development has mainly focused on their far-field behavior [1], antenna properties at length scales shorter than the radiation wavelength have raised substantial recent interest in the context of electric field enhancement and/or localization. Electric field distributions in the terahertz (THz) range, i.e., for wavelengths on the order of 100 μm, have been studied in detail with metallic electrodes, striplines, antennas, and resonator structures on solid substrates and semiconductor samples. Early studies have addressed such properties of electrically biased structures with gap sizes of up to 100 μm [2–4]. Motivated by applications in surface-enhanced Raman spectroscopy [5], THz imaging [6], THz high-field interactions [7], and generation of nanoscale photocurrents [8], subsequent work has focused on near-field effects at the sub-wavelength scale [7,9–19].

A quantitative investigation of near-field effects in THz antennas poses an experimental challenge due to the small length scales and the need for detection schemes with a high spatial resolution. In transmission geometries, the thickness of the substrate and/or sample underneath the antenna structures limits the spatial resolution as well. Near-field signatures have been studied by measuring the THz transmission through gaps in metallic structures [11,15,20] or by applying imaging techniques with a spatial resolution of up to a few micrometers [10,14,16,17]. Recent experimental work based on time-resolved imaging has addressed near-field properties in the gap of individual metallic dipole antennas [7,9]. In a variety of structures, pronounced local enhancements of the THz electric field by a factor of up to 50 have been observed at the surface of the structures and/or in transmission through sample layers of sub-micrometer thickness. THz electric-field distributions have also been a subject of simulations [12,18,19]. However, a direct comparison of theory and experiments has remained difficult.

#399462 https://doi.org/10.1364/OE.399462
Journal © 2020 Received 4 Jun 2020; revised 23 Jul 2020; accepted 27 Jul 2020; published 3 Aug 2020

Optics EXPRESS

In this paper, we study the near-field properties and electric-field enhancement of wide-gap bow-tie THz antennas (Figs. 1(a) and (b)) . The antennas with gap widths between 11 to 27 μm are designed for applications in nonlinear THz spectroscopy of soft matter, in particular liquids, in the femtosecond time domain. The antenna structure is typically located on the front window of a liquid-sample cell (Fig. 1(d)) and experiments are performed in transmission though the sample of some 10 μm thickness. In a pump-probe approach, the nonlinear response of the sample to the enhanced THz field is mapped by transmitting a femtosecond probe pulse through the antenna gap and the sample volume behind. In contrast to most antenna applications reported so far, the sample thickness and the spot diameter of the femtosecond probe pulses define particular experimental issues and call for an accurate characterization of the spatial and temporal properties of the THz field.

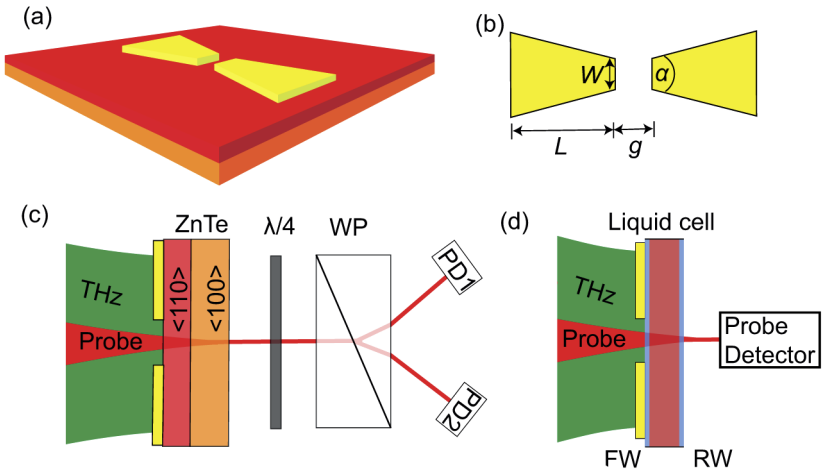

Fig. 1. **(a)** Schematic of a bow-tie antenna on a substrate consisting of a 10 μm thin ZnTe (110) crystal and a 500 μm thick ZnTe (100) substrate. **(b)** Structure and dimensions of the bow-tie antenna. The antenna consists of two arms of length L separated by the gap width g. The arms have a width W at the gap edges and an opening angle α. **(c)** Detection scheme for the enhanced THz electric field via EO sampling. The THz beam (green) and near-infrared probe beam (red) are focused by a parabolic mirror (effective focal length 25.4 mm) onto the antenna structure deposited on the ZnTe crystal. The THz electric field is read out by a detection system consisting of a quarterwave plate, a Wollaston prism (WP) and a pair of balanced photodetectors (PD1 and PD2). **(d)** Interaction geometry for pump-probe experiments on liquid samples with antenna-enhanced THz excitation. The THz electric field is enhanced by an antenna structure on the thin front window (FW) of the sample cell, e.g., a (sub-)micrometer thick silicon nitride membrane. The thickness of the liquid layer is on the order of 10 μm. The transmission change induced by the THz electric field is probed with a femtosecond pulse at higher frequency (RW: rear window).

For a quantitative spatially resolved measurement of electric field enhancements, antenna structures are deposited directly on a zinc telluride (ZnTe) crystal of approximately 10 μm thickness, thus mimicking the thickness of typical liquid samples. In this geometry, the THz near-field is detected in a temporally and spatially resolved way via electrooptic (EO) sampling (Fig. 1(c), [21]). This technique supports a high spatial resolution, only limited by the spot size of the probe beam and the thickness of the EO crystal. We first investigate the impact of varying gap widths and arm lengths on the electric-field enhancement and the resonance frequency of the antennas. Second, the lateral enhancement distribution across the antenna gap is studied with a

Optics EXPRESS

spatial resolution of $\lambda_{THz}/100$. The experimental results are reproduced by numerical solutions of the Maxwell equations for the particular antenna geometries.

2. Experimental

2.1. Design and fabrication

The resonant bow-tie antennas, schematically displayed in Fig. 1(a), were prepared by electron-beam lithography and deposited by thermal metal evaporation on a ZnTe crystal. The antennas consist of a 200 nm thick gold layer and a 3 nm thick layer of chromium to provide sufficient cohesion on the substrate.

Figure 1(b) shows the specific antenna design. The bow-tie antennas possess a fixed opening angle of $\alpha = 28°$ and a width W of 15 μm at the gap edges. Two sets of antennas were prepared. In the first set, the arm length L is varied between 50 and 65 μm, and the gap width g is fixed at 11 μm. In the second set, the gap width is varied between 12 and 27 μm, and the arm length is fixed at 53 μm. Studying these wide-gap antennas allows for a precise characterization of the antenna properties, including their resonance frequency, the electric-field enhancement at the center of the gap, and the enhancement distribution across the gap.

2.2. THz experiments and analysis

THz pulses were generated by difference frequency mixing in a GaSe crystal (thickness 500 μm) of broadband 25-fs near-infrared pulses from a Ti:sapphire oscillator/amplifier system working at a 1 kHz repetition rate [22]. The energy of the amplified 800-nm pulses was 0.5 mJ, their bandwidth (FWHM) approximately 45 nm. Before amplification, the optical phase and amplitude of part of the oscillator output is tailored with the help of an acoustooptic modulator (DAZZLER) to generate THz pulses with a spectrum centered at 0.7 THz. As schematically shown in Fig. 1(c), the generated THz beam is focused onto the antenna by an off-axis parabolic mirror of an effective focal length of 25.4 mm. The THz spot on the antenna structure has a diameter of some 500 μm, i.e., large compared to the antenna dimensions.

The THz field transmitted through the antenna gap is determined in amplitude and phase by EO sampling in the (110) ZnTe crystal [21,23], mounted on the passive 500 μm thick (100) ZnTe substrate with the same refractive index to avoid undesired reflections from the backside [24]. For sampling the THz waveform, a small fraction of the Ti:sapphire oscillator output serves as a linearly polarized probe pulse. To provide a high lateral resolution, the spot size of the probe beam is reduced to 3 μm (intensity decreased to $1/e^2$) by implementing a beam expander before focusing. The polarization change of the probe beam by the THz-driven EO effect in the thin (110) ZnTe crystal is measured with a detection scheme consisting of a quarter-wave plate, a Wollaston polarizer and two balanced Si photodiodes. The spatial resolution along the THz propagation direction is limited by the thickness of the ZnTe crystal of 10 μm whereas the lateral resolution of 3 μm is set by the spot size of the focused probe beam. The EO signal was calibrated in terms of the absolute THz field strength by measuring the energy of the THz pulses with a power meter and calculating the field strength. All measurements were performed in a nitrogen-purged chamber to avoid undesired interactions between the THz radiation and water vapor.

The experimental results were compared to numerical solutions of the Maxwell equations with the boundary conditions set by the metallic antenna structures and the ZnTe substrate. In a finite-element approach, we consider a geometry consisting of an upper domain representing the free space above the structure, a workplane containing the antenna, and a bottom domain representing the ZnTe crystal. The Maxwell equations were then solved with the COMSOL multiphysics software.

Optics EXPRESS

2.3. Electric-field enhancement

The electric-field enhancement in the antenna gap is derived from the comparison of two measurements (Fig. 2(c)); a reference measurement (black) with the spot of the probe beam far away from the antenna and a second equivalent measurement in the antenna gap (red). Figure 2(b) shows exemplary time traces of the transmitted THz field at the two positions. Figure 2(c) displays the corresponding frequency spectra obtained by a Fourier transform of the time-domain transients. Finally, the local-field enhancement in the frequency domain is obtained from the ratio of signal to reference spectrum, as presented in Fig. 2(d).

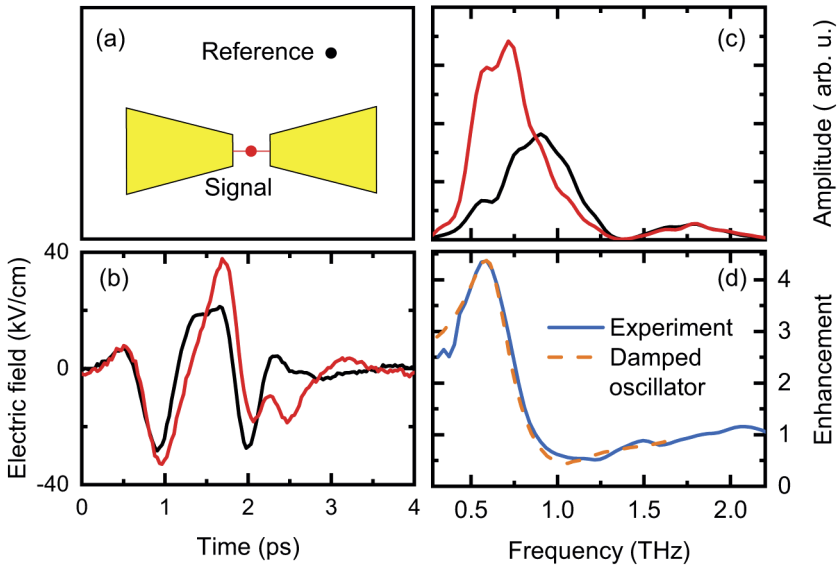

Fig. 2. **(a)** Schematic of spatially resolved EO sampling, showing the antenna structure (gap width 11 μm, arm length 65 μm) and two positions where signals and the reference THz transients are measured. **(b)** THz transients of signal (green line) and reference (black line) measured by electrooptic sampling. The electric field is plotted as a function of time. **(c)** Frequency spectra of the signal (green line) and reference (black line) transients from a Fourier transform of the time-domain signals. **(d)** Electric-field enhancement as a function of THz frequency. The enhancement (blue line, cf. Fig. 2(c)) is given by the ratio of signal to reference spectrum. The orange dashed line was calculated from a damped driven harmonic oscillator.

The enhancement spectrum possesses a distinct peak at the resonance frequency in the near field. Interestingly, the electric-field enhancement decreases below unity for frequencies larger than this resonance frequency and decays relatively slowly towards lower frequencies. These features of the line shape can be qualitatively accounted for by a damped driven oscillator model, presented as a dashed line in Fig. 2(d). This model was first used by Werley et al. [7].

3. Results

3.1. Impact of varying arm lengths and gap widths

Enhancement spectra for a spatial position at the center of the antenna gap were determined for bow-tie structures of varying gap widths and arm lengths. Figure 3 summarizes the experimental and calculated enhancement spectra. The calculated spectra are based on solutions of the Maxwell equations for the particular antenna geometry, using the dielectric functions of gold [25] and of

Optics EXPRESS

ZnTe [26]. The calculated enhancement spectra display a good agreement with the experimental results, possessing similar quality factors.

The resonance frequency and the maximum enhancement are extracted from the results. Figure 4(a) shows the resonance frequency as a function of the arm length. Both experiment (black rectangles) and calculation (red circles) indicate a distinct red-shift with increasing arm length. In Fig. 4(b), the resonance frequency is plotted as a function of the gap width, revealing a constant value of the resonance frequency. According to microwave theory [1], maximum scattering occurs if the arm length L is an integer multiple m of half the wavelength λ, i.e., $m \cdot \lambda/2 = L,\ m \in \mathbb{N}$. Thus, the resonance frequency is given by

$$\nu_0 = \frac{c}{2Ln_{\text{eff}}}, \tag{1}$$

where c is the vacuum speed of light and n_{eff} is an effective refractive index of the complex sample structure. The dash-dotted line in Fig. 4(a) represents a $1/L$ fit of the experimental result. We derive an effective refractive index of $n_{\text{eff}} = 4$, which is somewhat higher than the refractive index of the ZnTe crystal underneath ($n_{\text{ZnTe}} = 2.85$ [27]) [7]. This discrepancy suggests that the effective refractive index depends on the antenna dimensions, particularly the arm length, and points to a more complicated length dependence of the resonance frequency than assumed in Eq. (1). It should be emphasized that the results in Figs. 3 and 4 represent the near-field behavior of the THz antennas, in contrast to Ref. [10] where spectral shifts between resonance frequencies of the near- and the far-field have been analyzed.

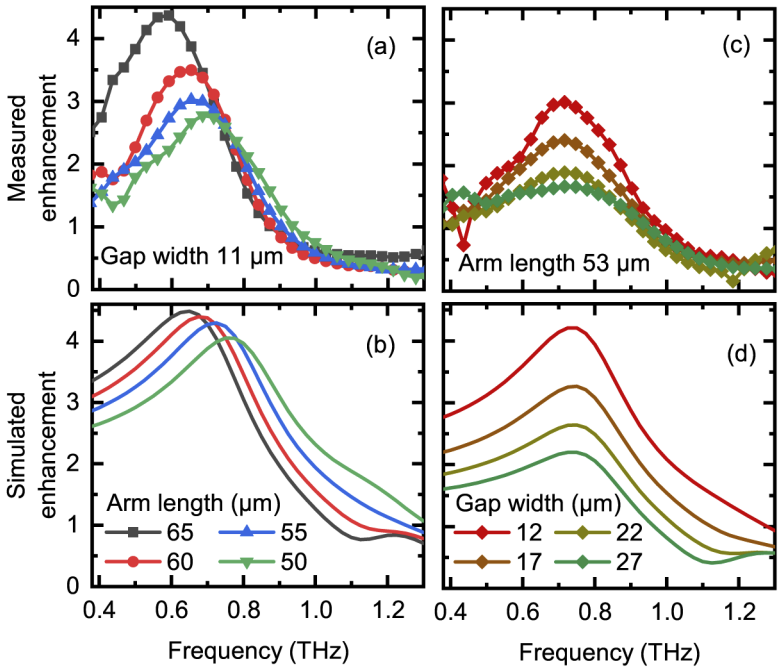

Fig. 3. **(a)** and **(b)** Frequency dependence of the electric-field enhancement in the antenna gap of bow-tie antennas with varying arm lengths and a gap width fixed at $g = 11\ \mu$m. **(c)** and **(d)** Frequency dependence of the electric-field enhancement of antennas with varying gap widths and an arm length fixed at $L = 53\ \mu$m. The results in Figs. 3(a) and (c) were obtained by experimentally imaging the near field of the antennas with EO sampling, the results in Figs. 3(b) and (d) by finite-element calculations.

Optics EXPRESS

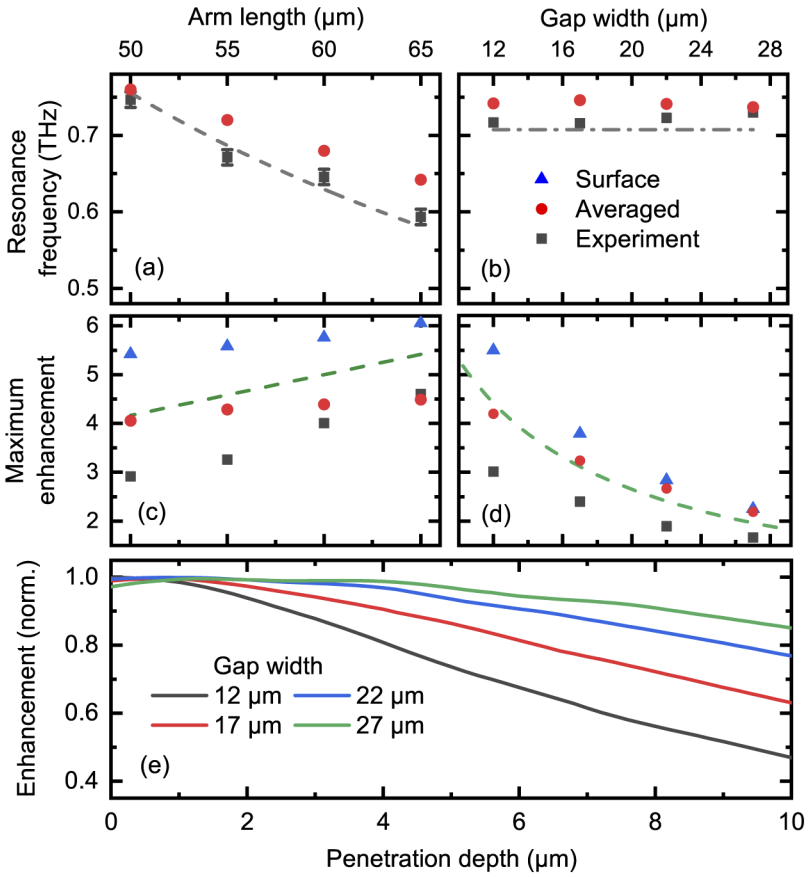

Fig. 4. Impact of bow-tie antenna dimensions on the THz resonance frequency and the maximum electric-field enhancement. **(a)** Resonance frequency as a function of the arm length. The gap width is fixed at 11 μm. The experimental results are represented by black rectangles and the corresponding simulation averaged over the thickness of the EO crystal by red circles. The dash-dotted line represents the $1/L$ behavior of a $\lambda/2$ dipole antenna. **(b)** Resonance frequency as a function of the gap width. The arm length is kept constant at 53 μm. **(c)** Maximum enhancement in the center of the gap as a function of the arm length (black symbols, gap width 11 μm). The blue triangles represent a simulation at the surface between the antenna arms, and the dashed line represents an L/g dependence. **(d)** Maximum enhancement as a function of the gap width. **(e)** Calculated decay of the electric-field enhancement in the center of the gap when penetrating into the substrate. The enhancement factors are normalized. The arm length is fixed at 53 μm.

Optics EXPRESS

Figure 4(c) shows the maximum enhancement as a function of the arm length. The data points (black symbols) represent the enhancement averaged over the thickness of the EO crystal of 10 μm. We observe a maximum enhancement of 4.5 for a bow-tie antenna with $L = 65$ μm and $g = 11$ μm. To analyze the impact of field averaging in the EO crystal, two types of simulations are performed. First, the calculated field enhancement is averaged over a thickness of 10 μm below the antenna gap (red circles), matching the experimental findings well. Second, the enhancement in an infinitesimally thin surface layer is calculated (blue triangles), revealing the electric-field enhancement before penetrating into the substrate. Such enhancement factors are significantly larger than the averaged values. The electric field enhancement calculated as a function of the penetration depth is displayed in Fig. 4(e). The spectra are normalized to their maxima, rendering a comparison for different gap widths possible. For small gap widths, the enhancement clearly decreases faster than for larger gaps. As a rule of thumb, the enhancement decreases by some 50% after penetrating a depth similar to the gap width.

Figure 4(d) displays the maximum enhancement as a function of the gap width. The electric-field enhancement increases with smaller gaps. The maximum enhancement at the center of the gap in Figs. 4(c) and 4(d) agrees with a basic capacitor-like model. The incoming THz electric field E_{THz} drives charge carriers to the ends of the antenna arms and induces an opposing electric field $-E_{\mathrm{THz}} = U_L/L$ along the antenna arms. Hence, the potential drop along an antenna arm equals the potential drop along the gap $U_L = -U_g$, resulting in an enhancement of

$$E_g/E_{\mathrm{THz}} = \frac{U_g L}{U_L g} = L/g. \tag{2}$$

This L/g dependence is plotted as a dashed line in Figs. 4(c) and 4(d). Further reduction of the gap width should result in stronger electric-field enhancement factors at the center of the antenna gap.

3.2. Lateral enhancement distribution along the antenna gap

Several studies, primarily of theoretical nature, have investigated the electric-field distribution across the gap of antenna structures and predict enhancement maxima at the antenna edges [12,18,19]. In most experiments, however, the antenna gap widths are chosen in the low micrometer or nanometer range, which has made an experimental verification of the calculated lateral variation of enhancement nearly impossible. Here, we determine the electric-field distribution across the gap of a wide-gap bow-tie antenna with an arm length of $L = 60$ μm and a gap width of $g = 22$ μm by spatially resolved EO sampling and compare the results to simulations. To spatially resolve the electric-field enhancement distribution, the probe beam with a spot size of 1/7 of the gap width is scanned laterally through the gap (cf. white dotted line in Fig. 5(b)). At the antenna edges one expects longitudinal polarization components of the THz field [28]. In the present EO sampling detection-scheme such components are absent in the measured signal. It should be noted that diffraction or clipping of the 800 nm probe occurs at positions closer than 3 μm from the antenna edges. Measurements at such positions are not included here.

Figure 5(a) shows a finite-element simulation of the two dimensional (2D) enhancement distribution of the antenna. The 2D map reveals various regions of enhancement, most prominently the gap. The experimental result in Fig. 5(c) (black symbols) demonstrates a moderate increase of enhancement towards the edges of the gap. This behavior is well reproduced by the calculations (red symbols). In absolute numbers, the maximum enhancement decreases from a value of approximately 3.5 at the edges of the gap to 2.3 in the center, the latter value being in good agreement with the gap width dependence presented in Fig. 4(d). A measurement of field enhancements in the regions of the antenna arms was impossible because of the very low transmission of the 800 nm probe beam through the gold layers. The simulations suggest enhancement factors on the order of one for the flat regions away from the edges.

Optics EXPRESS

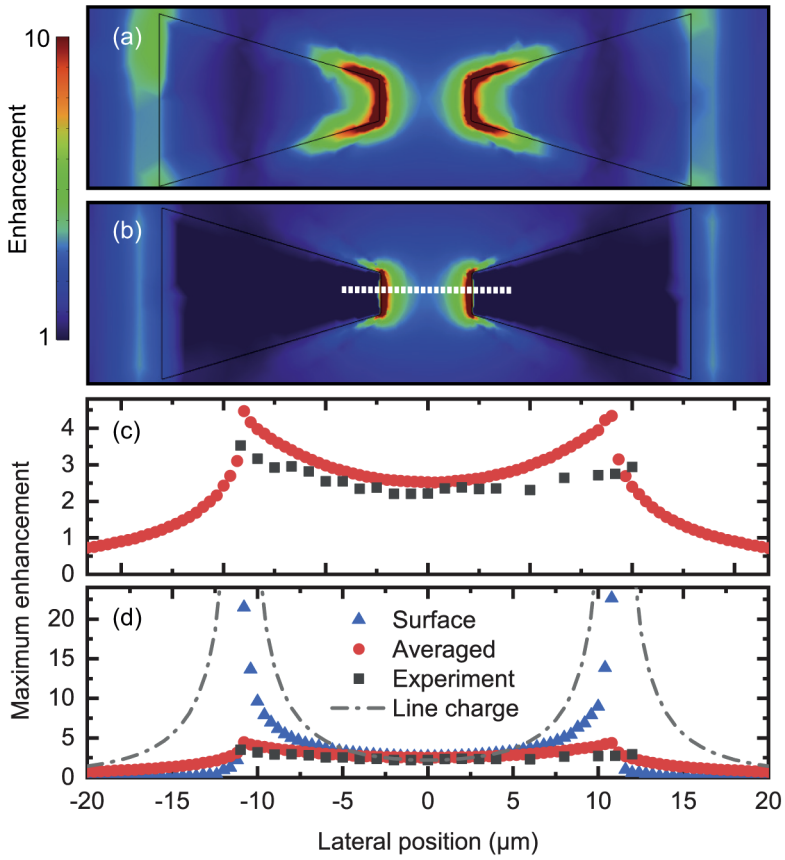

Fig. 5. **(a)** Simulated spatial distribution of the enhancement of the total THz electric field in a bow-tie antenna structure with $L = 53$ μm and $g = 22$ μm. **(b)** Simulated spatial distribution of the enhancement of the in-plane component of the THz electric field. The data and simulation results in Figs. 5(c) and (d) represent cuts along the white dashed line. **(c)** Electric-field enhancement at different lateral positions along the antenna gap at a frequency of 0.7 THz from experiment (black rectangles) and simulation (red circles). **(d)** Comparison of the results of Fig. 5(c) with the calculated enhancement at the surface (blue triangles) and a simple line-charge model (dash-dotted line).

Optics EXPRESS

In Fig. 5(d), the averaged field enhancement (black and red symbols) is compared to the calculated field enhancement at the surface (blue triangles). In the center, the calculated surface enhancement lies just slightly above the experimental value. This behavior is in line with the fact that the effect of field averaging over the 10 μm thickness of the EO crystal is minor for the 22 μm gap width investigated here. Towards the antenna edges, the calculated electric-field enhancement at the surface rises steeply and exhibits a divergent behavior at the edges. To comprehend the underlying mechanisms, a simple model of two oppositely charged wires in a distance of the gap width is considered. In this geometry, the charge density in the wires, assumed identical to the charge density of gold, determines the extremely high field enhancement close to the wires (dash-dotted line). At the gap center, this model gives an enhancement similar to the full simulation.

4. Conclusions

In conclusion, spatially resolved electrooptic sampling has provided detailed insight in the electric-field enhancement in THz bow-tie antennas designed for high-field THz experiments with soft-matter samples. Enhancement factors of up to 4.5, resonance frequencies in the 0.5 to 0.8 THz range, and spatial profiles of field enhancement within the antenna gaps were measured. Such results are fully accounted for by numerical solutions of the Maxwell equations by a finite-element approach. The results indicate that the antennas qualitatively behave like damped driven oscillators. Their resonance frequency is close to that of a $\lambda/2$ dipole antenna, while the electric-field enhancement factor at the center of the gap is essentially given by the ratio of the antenna arm length to the gap width. Within the antenna gap, the field enhancement displays a pronounced increase towards the edges. For a gap width of 22 μm, one finds a variation by a factor of approximately two.

The antenna structures studied here can be implemented on sample surfaces and/or thin sample windows and, thus, allow for optical experiments in a transmission geometry. In this way, the optical response of a micrometer-thick solid or liquid sample under the action of an enhanced THz field becomes accessible. Work along those lines is currently underway.

Funding

European Research Council (833365); Deutsche Forschungsgemeinschaft (WO 558/14-1).

Acknowledgment

This research has received funding from the European Research Council (ERC) under the European Union's Horizon 2020 research and innovation program (grant agreement No. 833365). M. W. acknowledges funding from Deutsche Forschungsgemeinschaft (grant agreement No. WO 558/14-1).

Disclosures

The authors declare no conflicts of interest.

References

1. C. A. Balanis, *Antenna Theory: Analysis and Design*, 2nd. ed. (Wiley, 1997).
2. S. E. Ralph and D. Grischkowsky, "Trap-enhanced electric fields in semi-insulators: The role of electrical and optical carrier injection," Appl. Phys. Lett. **59**(16), 1972–1974 (1991).
3. Y. Cai, I. Brener, J. Lopata, J. Wynn, L. Pfeiffer, and J. Federici, "Design and performance of singular electric field terahertz photoconducting antennas," Appl. Phys. Lett. **71**(15), 2076–2078 (1997).
4. M. Bieler, G. Hein, K. Pierz, U. Siegner, and M. Koch, "Ultrafast electric field measurements in semiconductors by spectral intergration over electric field-induced Franz-Keldysh oscillations," Appl. Phys. Lett. **87**(4), 042102 (2005).
5. K. A. Willets and R. P. Van Dyne, "Localized surface plasmon resonance spectroscopy and sensing," Annu. Rev. Phys. Chem. **58**(1), 267–297 (2007).

Optics EXPRESS

6. W. L Chan, J. Deibel, and D. M. Middleman, "Imaging with terahertz radiation," Rep. Progr. Phys. **70**(8), 1325–1379 (2007).
7. C. A. Werley, K. Fan, C. Strikwerda, S. Teo, X. Zhang, R. D. Averitt, and K. A. Nelson, "Time-resolved imaging of near-fields in THz antennas and direct quantitative measurement of field enhancements," Opt. Express **20**(8), 8551–8567 (2012).
8. D. R. Ward, F. Hüser, F. Pauly, J. C. Cuevas, and D. Natelson, "Optical rectification and field enhancement in a plasmonic nanogap," Nat. Nanotechnol. **5**(10), 732–736 (2010).
9. M. Savoini, S. Grübel, S. Bagiante, H. Sigg, T. Feurer, P. Beaud, and S. L. Johnson, "THz near-field enhancement by means of isolated dipolar antennas: the effect of finite sample size," Opt. Express **24**(5), 4552–4562 (2016).
10. A. Bhattacharya, G. Goergiou, S. Sawallich, C. Matheisen, M. Nagel, and J. Gómez Rivas, "Large near-to-far field spectral shift for terahertz resonances," Phys. Rev. B **93**(3), 035438 (2016).
11. A. Halpin, C. Mennes, A. Bhattacharya, and J. Gómez Rivas, "Visualizing near-field coupling in terahertz dolmens," Appl. Phys. Lett. **110**(10), 101105 (2017).
12. N. T. Yardimci and M. Jarrahi, "High sensitivity terahertz detection through large-area plasmonic nano-antenna arrays," Sci. Rep. **7**(1), 42667 (2017).
13. A. Bhattacharya and J. G. Rivas, "Full vectorial mapping of the complex electric near-fields of THz resonators," APL Photonics **1**(8), 086103 (2016).
14. O. Mitrofanov, I. Khromova, T. Siday, R. J. Thompson, A. N. Ponomarev, I. Brener, and J. L. Reno, "Near-field spectroscopy and imaging of subwavelength plasmonic terahertz resonators," IEEE Trans. Terahertz Sci. Technol. **6**(3), 382–388 (2016).
15. J. Wallauer, A. Bitzer, S. Waselikowski, and M. Walther, "Near-field signature of electromagnetic coupling in metamaterial arrays: a terahertz microscopy study," Opt. Express **19**(18), 17283–17292 (2011).
16. N. Kumar, A. C. Strikwerda, K. Fan, X. Zhang, R. D. Averitt, P. C. M. Planken, and A. J. L. Adam, "THz near-field Faraday imaging in hybrid metamaterials," Opt. Express **20**(10), 11277–11287 (2012).
17. F. Blanchard, A. Doi, T. Tanaka, H. Hirori, H. Tanaka, Y. Kadoya, and K. Tanaka, "Real-time terahertz near-field microscope," Opt. Express **19**(9), 8277–8284 (2011).
18. X. Zhao, J. Zhang, K. Fan, G. Duan, G. D. Metcalfe, M. Wraback, X. Zhang, and R. D. Averitt, "Nonlinear terahertz metamaterial perfect absorbers using GaAs," Photonics Res. **4**(3), A16–A21 (2016).
19. J. Zhang, X. Zhao, K. Fan, X. Wang, G.-F. Zhang, K. Geng, X. Zhang, and R. D. Averitt, "Terahertz radiation induced sub-cycle field electron emission across a split-gap dipole antenna," Appl. Phys. Lett. **107**(23), 231101 (2015).
20. J. G. Rivas, C. Schotsch, P. H. Bolivar, and H. Kurz, "Enhanced transmission of THz radiation through subwavelength holes," Phys. Rev. B **68**(20), 201306 (2003).
21. Q. Wu and X.-C. Zhang, "Free-space electrooptic sampling of terahertz beams," Appl. Phys. Lett. **67**(24), 3523–3525 (1995).
22. R. A. Kaindl, F. Eickemeyer, M. Woerner, and T. Elsaesser, "Broadband phase-matched difference frequency mixing of femtosecond pulses in GaSe: Experiment and theory," Appl. Phys. Lett. **75**(8), 1060–1062 (1999).
23. P. C. M. Planken, H.-K. Nienhuys, H. J. Bakker, and T. Wenckebach, "Measurement and calculation of the orientation dependence of terahertz pulse detection in ZnTe," J. Opt. Soc. Am. B **18**(3), 313–317 (2001).
24. T. Elsaesser, K. Reimann, and M. Woerner, *Concepts and Applications of Nonlinear Terahertz Spectroscopy* (Morgan & Claypool Publishers, 2019).
25. M. A. Ordal, R. J. Bell, R. W. Alexander, L. L. Long, and M. R. Querry, "Optical properties of fourteen metals in the infrared and far infrared: Al, Co, Cu, Au, Fe, Pb, Mo, Ni, Pd, Pt, Ag, Ti, V, and W," Appl. Opt. **24**(24), 4493–4499 (1985).
26. A. Manabe, A. Mitsuishi, and H. Yoshinaga, "Infrared lattice reflection spectra of II-VI semiconductors," Jpn. J. Appl. Phys. **6**(5), 593–600 (1967).
27. D. T. F. Marple, "Refractive index of ZnSe, ZnTe, and CdTe," J. Appl. Phys. **35**(3), 539–542 (1964).
28. M. Woerner, C. Somma, K. Reimann, T. Elsaesser, P. Q. Liu, Y. Yang, J. L. Reno, and I. Brener, "Terahertz driven amplification of coherent optical phonons in GaAs coupled to a metasurface," Phys. Rev. Lett. **122**(10), 107402 (2019).